RSC Advances

ROYAL SOCIETY OF CHEMISTRY

www.rsc.org/advances

Graphical Abstract

Cobalt supported on metal-doped ceria catalysts (M = Zr, Sn and Ti) for NO oxidation

Yang Yu[1,2], Lei Zhong[1,2], Jie Ding[1,2], Wei Cai [1,2], Qin Zhong* [1,2]

1 School of Chemical Engineering, Nanjing University of Science and Technology, Nanjing 210094, PR China.

2 Nanjing AIREP Environmental Protection Technology Co., Ltd, Nanjing, Jiangsu 210091, PR China.

This research probed different doping cations on the activities of ceria-based solid solutions supported cobalt oxides for NO oxidation. The detailed properties of the catalysts were investigated and the results showed that the higher activity depended on higher amount of finely dispersed cobalt species, more oxygen vacancy and excellent redox ability.

* Corresponding author.Tel./fax:+86 25 84315517

E-mail: zq304@mail.njust.edu.cn.

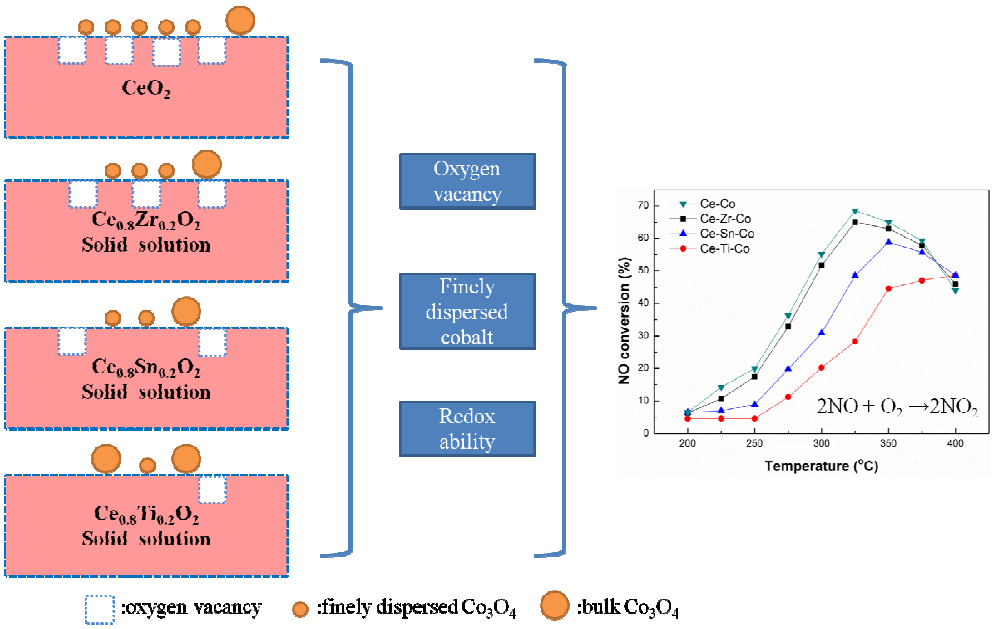

Cobalt supported on metal-doped ceria catalysts (M = Zr, Sn and Ti) for NO oxidation

Yang Yu[1,2], Lei Zhong[1,2], Jie Ding[1,2], Wei Cai [1,2], Qin Zhong* [1,2]

1 School of Chemical Engineering, Nanjing University of Science and Technology, Nanjing 210094, PR China.

2 Nanjing AIREP Environmental Protection Technology Co., Ltd, Nanjing, Jiangsu 210091, PR China.

Abstract: A series of ceria oxides doped with 20 mol.% of Zr, Sn and Ti were prepared by citric sol-gel method throughout the thermal decomposition of the corresponding metallic propionates. Furthermore, cobalt oxides were loaded on the supports by a one-step sol-gel method. The results showed solid solution when doping with Zr and Ti and SnO_2 surface segregation in the case of Sn. We demonstrated that cobalt dispersion states was influenced by the doping metals. Ce-Co metal-oxides catalyst possessed higher amount of finely dispersed cobalt species, more oxygen vacancy and excellent redox ability. These features may be responsible for improving the catalytic activity of Ce-Co metal-oxides for NO oxidation.

Keywords: Ceria-based solid solution; Dopant; selective catalytic oxidation; NO

* Corresponding author.Tel./fax:+86 25 84315517
E-mail: zq304@mail.njust.edu.cn.

1. Introduction

Development of methods to control NO_x emission has been an active research area [1] because NO_x are associated with acid deposition, photochemical smog, and ozone depletion. The catalytic oxidation of NO to NO_2 is a key step for many NO_x removal techniques, such as fast selective catalytic reduction (fast SCR) [2], NO_x storage-reduction (NSR) [3], continuously regenerating trap (CRT) [4], and the wet scrubbing method [5]. Therefore, many efforts have been focused on developing eligible catalysts for NO oxidation [6-10].

Ceria (CeO_2) is one of the most reactive rare-earth oxides and attracts much attention due to its unique application in catalysts [6, 8, 9]. The catalytic properties of ceria are considered to originate from the Ce^{4+}/Ce^{3+} redox cycle. It is affected by various structural factors, such as composition modification, large surface area, preferential exposure of reactive facets and the oxygen vacancies concentration on its surface [11-14]. However, it is well known that sintering effect often occurs when pure CeO_2 is used at high temperature, resulting in the decrease of specific surface area and oxygen storage capacity (OSC) [15]. Many researches have been performed by incorporating foreign metal cations into the lattice of CeO_2 to restrain this effect. These metal cations mainly contain three categories : (i) M^{2+} (Ca^{2+} [16], Mg^{2+} [17]), (ii) M^{3+} (Al^{3+}, Ga^{3+}, In^{3+} [18, 19]) and (iii) M^{4+} (Zr^{4+} [6], Sn^{4+} [20], Ti^{4+} [21], Mn^{4+} [22], Hf^{4+} [23]). Recently, our lab [24] prepared a series of $Cr/Ce_xZr_{1-x}O_2$ catalysts used for NO oxidation and found that the Zr-rich samples showed higher activity than

Ce-rich sample; Dobrosz-Gómez et al. [25] prepared a series of $Au/Ce_xZr_{1-x}O_2$ used them in CO oxidation and the $Au/Ce_{0.75}Zr_{0.25}O_2$ exhibited the best catalytic performance; Ayastuy et al. [26] reported that $Ce_{0.95}Sn_{0.05}O_2$ had the highest activity in CO oxidation reaction among the $Ce_xSn_{1-x}O_2$ catalysts. According to the above-mentioned literatures, we could find that the previous works were mainly focused on investigating the catalytic property of the catalyst by modulating the ratio of Ce/M. However, there were almost few reports which focus on changing the doped metal cation of $Co_3O_4/Ce_xM_{1-x}O_2$ for a comparative study.

It was widely reported that cobalt oxide based catalysts were potential candidate for NO oxidation. Wen et al. studied series of $La_{1-x}Ce_xCoO_3$ perovskite oxide catalysts for nitrogen monoxide oxidation, and reported approximately 80 % conversion on $La_{0.8}Ce_{0.2}CoO_3$ at 300 ^oC [27]. TiO_2 and SiO_2 supported Co_3O_4 catalysts were studied for NO oxidation by Irfan et al. [28]. They reported maximum of 69 % conversion on Co_3O_4/SiO_2 at 300 ^oC with high space velocity condition. Recently, Kim et al. studied NO oxidation on supported cobalt oxide synthesized by conventional wet impregnation method using various supports including CeO_2, SiO_2, ZrO_2, TiO_2 and SiO_2, and reported that CeO_2 supported catalyst exhibits better activity. They reported approximately 70 % conversion at about 270 ^oC on Co-ceria and found that surface area of CeO_2 played an important role on catalytic activity [29]. As it was reported in the previous literatures, the support was crucial for the dispersion of active species, however, few reports discussed the different role of cobalt species in the process of NO oxidation.

In the present work, ceria doped with Zr^{4+}, Sn^{4+}, Ti^{4+} were used as supports to prepare cobalt-based catalysts and the obtained samples have been studied systematically by means of XRD, LRS, UV-vis DRS, TEM, N_2-physisorption, H_2-TPR, XRF, XPS and NO + O_2 model reaction. The study was mainly focused on understanding the influence of dopant on the structure, texture, reduction, dispersion of cobalt species, oxygen vacancies, adsorption properties and catalytic performance of the obtained samples.

2. Experimental Section

2.1. Preparation of the catalysts

The $Ce_{0.8}M_{0.2}O_2$ (M = Zr^{4+}, Sn^{4+} and Ti^{4+}) solid solutions (Ce:M = 4:1 mloar ratio) were prepared by sol-gel method. The Ce, Zr, Sn and Ti sources were $Ce(NO_3)_3 \cdot 6H_2O$, $ZrOCl_2$, $SnCl_4$ and $TiCl_4$. The requisite quantity of Ce and M sources with citric acid (citric acid/(Ce + M) = 2) were added into distilled water to form solution. The above two solutions (Ce and M) together with citric acid were mixed together and stirred for 2 h. After that the mixture was heated at 90 ^oC under stirring until it became a viscous gel and dried at 120 ^oC for 12 h then the obtained solid was calcined in air at 500 ^oC for 4 h. In addition, pure CeO_2 was prepared via the same procedure for comparison. These synthesized samples were CeO_2, $Ce_{0.8}Zr_{0.2}O_2$ (hereafter denoted as Ce-Zr), $Ce_{0.8}Sn_{0.2}O_2$ (hereafter denoted as Ce-Sn), $Ce_{0.8}Ti_{0.2}O_2$ (hereafter denoted as Ce-Ti) supports.

The CoO_x/S (S = CeO_2, Ce-Zr, Ce-Sn, Ce-Ti) catalysts were prepared by one-step

sol-gel method. The Co source was $Co(NO_3)_2 \cdot 6H_2O$. The Ce, M (M = Zr, Sn and Ti) and Co solution with citric acid (citric acid/(Ce + M + Co) = 2) were mixed together and stirred for 2 h. After that the mixture was heated at 90 ^oC under stirring until it became a viscous gel and dried at 120 ^oC for 12 h then the obtained solid was calcined in air at 500 ^oC for 4 h. These catalysts were denoted as Ce-Co, Ce-Zr-Co, Ce-Sn-Co and Ce-Ti-Co, respectively.

2.2. Sample characterization

The powder XRD patterns were recorded on a Beijing Purkinjie general instrument XD-3 X-ray diffraction using Cu-$K\alpha$ radiation at 36 kV and 20 mA (2θ from 5^o to 80^o). The scanning speed is 8^o min^{-1} and the step value is 0.04^o. The average grain sizes of the catalysts were calculated using the Scherer's formula, Eq.(1):

$$D = \frac{K\lambda}{\beta \cos\theta} \quad (1)$$

where D is the average crystallite size; K is a constant; λ is the wavelength of the X-ray radiation (Cu $K\alpha$= 0.1541 nm); β is the full width at half-maximum (FWHM) of the diffraction peak (the corrected β equaling to the measured width (β_M) minus the instrument width (β_S)); θ is the diffraction angle. After correction, the formula is as shown in the following equation:

$$D = \frac{0.89*0.1506}{\frac{(\beta-0.09)}{180}*\pi*\cos\theta} \quad (2)$$

Laser Raman spectra (LRS) were recorded on a Renishaw Invia Raman Microscope with Ar^+ radiation (514 nm). The laser light was focused onto the samples by using a microscope equipped with a 6100 objective lens.

Diffuse reflectance spectroscopy (DRS) was carried out on a Shimadzu UV-2550 UV-vis spectrophotometer. $BaSO_4$ was the reference sample and the spectra were recorded in the range of 200-800 nm.

The micromorphology of the catalysts was examined on a JEOL JEM-2100 transmission electron microscope (TEM), and the sample was deposited on a copper mesh by means of dipcoating. The acceleration voltage is 200 kV.

Specific surface areas of the different catalysts were determined by N_2 adsorption-desorption measurements at -196 ^oC by employing the Brunauer-Emmet-Teller (BET) method (Gold App V-sorb 2800 p), and the pore volume and pore size of the samples were calculated by Barrett-Joyner-Halenda (BJH) method. The systematic error calculated for BET surface area, pore volume and pore size was given with the accuracy at ±5 $m^2\ g^{-1}$, ±5 $mm^3\ g^{-1}$ and ±0.5 nm. Prior to N_2 adsorption, the sample was outgassed at 200 ^oC for 12 h to desorb moisture adsorbed on the surface and inside the porous network.

Hydrogen temperature programmed reduction (H_2-TPR) was performed in a quartz U-tube reactor on an automated chemisorption analyzer (Quantachrome Instruments) by the GC method. About 100 mg sample was pretreated in N_2 stream at 600 ^oC for 0.5 h. As the sample was cooled downed to 50 ^oC, switched N_2 to H_2-N_2 mixture gas (10 % H_2, v/v) at a flow rate of 70 ml min^{-1}. H_2-TPR was performed by heating the sample from 50 to 700 ^oC, at the same time, the consumption of H_2 was detected by a thermal conductivity detector (TCD).

X-ray photoelectron spectra (XPS) was performed on a Thermo ESCALAB 250

(USA) apparatus with Al Kα X-rays (hv = 1486.6 eV) radiation operated at 150 W to investigate the surface atomic concentrations and the oxidation state distribution of the elements in the samples. The samples were compensate for charging with low-energy electron beam, and the peak of C 1s (Binding Energy = 284.4 eV) was used to correct for sample charging. This reference gave BE values with an accuracy ±0.1 eV. And the atomic surface ratios of the corresponding species were given with the accuracy at ±0.1 %. The penetration depth of the XPS probe is 10 nm.

X-ray fluorescence spectra (XRF) were carried out on an FL3-TCSPC apparatus to determine the bulk composition of these catalysts. The X-ray tube was operated at 60 kV and 20 mA. The accurate measurement mode was adopted to determine the contents of Co, Ce, Zr, Sn and Ti elements of these catalysts.

2.3. Catalytic testing

The catalytic oxidation of NO was performed in a fixed-bed flow microreactor under atmospheric pressure. Typically, 300 mg sample (sieve fraction of 40-60 mesh) was placed in a quartz reactor (6.8 mm i.d.); the reactant gas mixture (390 ppm NO, 8 % O_2, N_2 balance) was fed to the reactor with a total flow rate of 100 mL min^{-1}, corresponding to a gas hour space velocity (GHSV) of 35400 h^{-1}. The steady-state tests were conducted isothermally every 25 ^oC from 200 to 400 ^oC and the gas products (after 90 min reaction) were analyzed by a Ecom-JZKN flue gas analyzer (Germany). The NO conversion is defined as:

NO conversion = $(NO_{in} – NO_{out})/NO_{in}$*100 %.

3. Result and discussion

3.1. Catalytic activity of ceria-based mixed oxides (NO oxidation)

Fig.1

The profiles for NO conversion as a function of reaction temperature over these catalysts were present in Fig. 1a and b. For the Co-containing samples (Fig. 1a), the sequence of catalytic activity expressed as NO conversion is Ce-Co > Ce-Zr-Co > Ce-Sn-Co > Ce-Ti-Co. In contrast, the pure CeO_2 and CeO_2-MO_x (M = Zr^{4+}, Sn^{4+} and Ti^{4+}) samples were also prepared to evaluate the catalytic activity. Although the catalytic activity of all the supports is low, modified supports have relative higher activity than pure CeO_2. In general, the Co-containing samples shows higher catalytic activity than the supports, indicating Co species play an important role in the NO oxidation process.

3.2. Structural characteristics (XRD, LRS, UV-vis DRS and TEM)

Fig. 2

Fig. 2 shows the XRD patterns of these samples. It could be seen that all the diffraction peaks of these samples except Ce-Sn were characteristic of typical cubic fluorite phase of ceria (PDF-ICDD 34-0394). The characteristic lines attributed to ZrO_2 and TiO_2 were absent, the diffraction peaks of Ce-Zr and Ce-Ti shifted to high

angle direction slightly and the peaks became wider compared to CeO_2, which indicated that Zr^{4+} and Ti^{4+} were successfully doped into the lattice of CeO_2 to form uniform solid solutions. As for Ce-Sn, the diffraction peak of SnO_2 was observed, showing the absence of solid solution or little solid solution forming. In contrast, the Ce-Sn-Co sample showed no SnO_2 peak and the (1 1 1) peak of CeO_2 shifted to higher angle, this phenomenon indicated the adding Co could contribute to the forming of solid solution. The grain sizes of these samples are summarized in Table 1. The grain sizes of Ce-Zr, Ce-Sn and Ce-Ti were smaller than CeO_2, suggesting that the introduction of Zr^{4+}, Sn^{4+} and Ti^{4+} inhibited the crystal growth of the cubic phase [21]. After introducing of cobalt, the grain sizes decreased slightly compared to their corresponding supports except for Ce-Ti-Co. This phenomenon was probably due to the incorporation of monolayer cobalt into the surface/subsurface layers of these supports [30]. In addition, all the Co supported catalysts showed no peaks for crystalline cobalt oxides, indicating that cobalt oxide species were highly dispersed and/or present as small clusters and/or form solid solution which were difficult to be detected due to the limitation of XRD.

Table 1

Laser Raman spectroscopy is an intriguing tool to analyze the structural properties of oxide materials particularly nanostructured ceria-based solid solutions. The LRS of the supports are shown in Fig. 3a. The band at 464 cm^{-1} was the characteristic of the cubic fluorite structure of CeO_2 [31]. The observed shift and broadening of the F_{2g}

peaks in the 464 cm^{-1} was attributed to the change in the M-O vibration which accounted for the difference in the ionic radius of the dopants [32]. In our case, the observed decrease in the ceria particle size in the doped samples calculated by the Scherrer equation (Table 1) could agree with the shift and/or broadening of the F_{2g} peak. The Raman lines assigned to MO_2 (M = Zr^{4+}, Sn^{4+} and Ti^{4+}) were not observed. This results also confirmed that the doped cations entered the crystal lattice of CeO_2 which was in line with XRD results.

For the catalysts, the Raman lines of cobalt species were absent in all of the samples. In addition, the main band of these catalysts were red or blue shift in contrast to their support. This phenomenon could be explained be two reasons. One is that the existence of an interaction between support and the active species [33]. The other reason may be the incorporation of monolayer cobalt into the surface/subsurface layers of these supports, which was in consistent with XRD results.

Apart from the main peak of CeO_2, a new band II appeared at ca. 570 to 630 cm^{-1}, ascribing to the intrinsic oxygen vacancies [34]. They were very essential for absorption/dissociation of oxygen molecule during the catalytic oxidation reactions, which in turn could affect the catalytic activity of the catalysts [35]. Since the band II was related to oxygen vacancies, and the band I was the main band of these samples, the area ratio of A_{II}/A_I could reflect the concentration of oxygen vacancies. We could see from Table 1 that the Ce-Co had higher amount of oxygen vacancies.

Fig. 3

UV-vis DRS technique is effectively used for the study of metal oxides to obtain information about the charge transfer transitions. Ceria exhibited strong absorption below 400 nm caused by charge transfer bands. DR spectra of these samples are presented in Fig. 4. Three characteristic bands of ceria corresponding to the $O^{2-} \rightarrow Ce^{3+}$ and $O^{2-} \rightarrow Ce^{4+}$ charge transfer bands and inter-band transitions in the wavelength range 250-340 nm were observed for all samples [36, 37]. The absorption band observed at ca. 470 nm can be attributed to the $^1A_{1g} \rightarrow {}^1T_{1g}$ forbidden d-d transitions of Co^{3+} in its octahedral sites [38]. The peak observed at ca. 750 nm corresponded to Co^{2+} ions in its tetrahedral geometry [39]. It was confirmed that the evidence of the Co^{3+} and Co^{2+} species from DRS study was in accordance with H_2-TPR and XPS results.

Fig. 4

TEM was used to investigate the morphology and microstructure of the sample. Fig. 5 shows the TEM and HR-TEM imagines of these catalysts. From TEM imagines, we could clearly see that the particles of all the catalysts were irregular. It could be seen from the HRTEM imagines that these irregular imagines were comprised of many small particles with a crystallite size of 3-5 nm, and there were clear voids with diameter 3-5 nm among the small particles, revealing the mesostructure of the CeO_2 particles. Furthermore, the absence of Co-related particles' lattice in HRTEM images suggested a good dispersion of CoO_x

crystallites. From HRTEM, the interplanar distance of lattice fringes was 0.312 nm corresponding to (1 1 1) crystallographic plane of CeO_2. [40]. In contrast, the fringes of Ce-M-Co (M = Zr^{4+}, Sn^{4+} and Ti^{4+}) were little lower than 0.312 nm, indicating the forming of Ce-M solid solution. The results were consistent with XRD and Raman results.

Fig. 5

3.3. Textural characterization (N_2-physisorption)

The N_2 adsorption-desorption isothermal plots and the corresponding BJH pore size distribution curves of these samples were displayed in Fig. 6. It could be seen from Fig. 6a that all these samples were of classical type IV as defined by IUPAC and exhibited hysteresis loops of type H3, which indicated that these samples contained mesopores (2-50 nm) with narrow slit-like shapes [41]. The pore size distribution curves suggested that all the samples had defined mesoporosities. The pore size at the maximum probability of the catalysts was 6.9, 11.3, 10.8 and 13.8 nm for Ce-Co, Ce-Zr-Co, Ce-Sn-Co and Ce-Ti-Co, respectively. The BJH pore size distribution plots of the various catalysts possessed nonuniform mesopore size distribution.

The BET surface area, pore volume and pore size of these catalysts are summarized in Table 2. Compared with Ce-Co, when the foreign metal cations were doped into the lattice of CeO_2 (formed Ce-Zr, Ce-Sn, and Ce-Ti solid solutions), both the specific surface area and pore volume increased. These

changes may be related to the grain size of the samples to some extent. In other words, the incorporation of Zr^{4+}, Sn^{4+} and Ti^{4+} into the lattice of CeO_2 could improve the texture property effectively. In order to explore the thermal stability, all of the four supports were calcined in air at 800 ^oC for 4 h in flowing air, and then, BET measurements were carried out, and the specific surface areas were summarized in Table S1. Compared with pure CeO_2, the degree of sintering (i.e. S_{BET} (500) - S_{BET} (800)/S_{BET} (500)) was smaller when Zr^{4+}, Sn^{4+} and Ti^{4+} incorporated into the lattice of CeO_2. It indicated that the ability of anti-sintering of CeO_2 was enhanced with the introduction of these foreign metal cations.

Fig. 6

Table 2

3.4. Reduction properties of the catalysts (H_2-TPR)

H_2-TPR tests were performed to study the reducibility of these catalysts. Fig. 7 shows that the shape of these TPR profiles is very different, indicating the support has an important effect on the dispersion of Co_3O_4. With respect to the reduction steps of Co_3O_4, they were rather controversial in literature. Arnoldy and Moulijn [42] observed a single step for the reduction of Co_3O_4, while many others [43-45] reported that the reduction of Co_3O_4 was a two-step process, involving in the reduction to CoO. The results here clearly showed that the reduction behaviors of Co_3O_4 strongly depended on preparation, catalyst composition and dispersion behavior, consistent

with the finding of Spadaro et al. [46]. Large particles of Co_3O_4 were often reduced directly to metallic Co in a single step, while fine particles of Co_3O_4 that interacted with ceria seemed to get reduced in two steps. The first step was generally promoted by component interaction between them, possibly ascribed to the lengthening in the Co-O bond, while the second step was perhaps delayed by the stabilization effect of ceria to cobalt ions, similar assignment has ever reported by Martínez-Arias et al. for CuO/CeO_2 system [47]. On the basis, the following assignments were made for the reduction of cobalt species in respect of the temperature ranges:

Range I (below 320 ^oC): reduction of the surface adsorbed oxygen species (indicated as peak α for Ce-Co catalyst);

Range II (320-420 ^oC): reduction of Co^{3+} at the interface between Co_3O_4 and CeO_2 to Co^{2+} (peak β);

Range III (420-500 ^oC): reduction of independent Co_3O_4 that weakly interacts with CeO_2 directly to Co (peak γ);

Range IV (500-700 ^oC): reduction of Co^{2+} interacting with CeO_2 to Co (peak θ);

Since the peak in Range II were related to the finely Co_3O_4 species and Range III were independent or bulk-like Co_3O_4 phase, we could infer the dispersion state of Co_3O_4 phase from the intensity of this peak. As shown the dotted box in Fig. 7, the peak area ratio of A_β/A_γ was 1.8, 0.5, 0.4 and 0.3, referring to Ce-Co, Ce-Zr-Co, Ce-Sn-Co and Ce-Ti-Co, respectively. The reduction temperature of peak β and peak γ shifted to higher temperature in contrast with Ce-Co. Thus it could be seen that the support had significant effect on the reduction properties and component dispersion.

Combined with the activities performance, we could infer that highly dispersed Co_3O_4 possessed better catalytic activity. Similar conclusions were reported by Luo et al. [13], they found that the finely dispersed CuO species had higher activity compared to bulk CuO species.

Fig. 7

3.5. Bulk and surface analysis of the catalysts (XRF and XPS);

The bulk composition of these catalysts were characterized by XRF. As shown in Table 3, the chemical composition of the catalysts matched well the intended one, evidencing that the thermal decomposition of the propionates method allowed obtaining materials with a controlled stoichiometry. XPS was performed in order to illuminate the surface composition and the chemical state of the elements existing in the catalysts. The deconvoluted photoelectron spectra of the Ce 3d, Co 2p, O 1s, Zr 3d, Sn 3d and Ti 2p are shown in Fig. 8. Ce 3d core level spectra (Fig. 8a) for all the samples were deconvoluted into eight contributions. The spin-orbit splitting of Ce $3d_{5/2}$ and Ce $3d_{3/2}$ was 18.5 eV for all the samples, which was in good agreement with literature [48]. The u''' satellite peak at about 916.5 eV was the fingerprint of Ce^{4+} state, and its high intensity and area suggested that the main part of the ceria was in Ce^{4+} oxidation state. After deconvolution the appearance of bands labeled u' and v' were typical for Ce^{3+} ions, which suggested that both oxidation states Ce^{4+} and Ce^{3+} coexist in the surfaces of samples [48]. The enhancement of unhomogeneity of the Ce

and M (M = Zr, Sn and Ti) atoms could improve the valence change of the Ce (Ce^{4+} → Ce^{3+}) [6]. Another reason was probably due to the substitution of Ce^{4+} by M (M = Zr^{4+}, Sn^{4+} and Ti^{4+}) ions partly in the calcination process. The spontaneous transformation of Ce^{4+} (r_{Ce4+} = 0.97 Å) ions to the larger Ce^{3+} (r_{Ce3+} = 1.10 Å) could compensate for this lattice contraction. The relative intensities of u' to v' to the whole eight bands were 12.88 %, 20.35 %, 23.58 % and 30.42 %, referring to Ce-Co, Ce-Zr-Co, Ce-Sn-Co and Ce-Ti-Co, respectively, which was shown in Table 3. Obviously, the surface ratios of Ce^{3+} to (Ce^{3+} + Ce^{4+}) on the catalysts were higher after introduction M ions, indicating the introduction of M could cause charge imbalance and forming the Ce-M solid solution. It was obvious that the binding energy of Ce shifted to the high field after introduction of other cations. The reason could be explained by the density of electron cloud decreased as the addition of strong electrophilic M cations (Electronegativity: Zr = 1.33, Sn = 1.96 and Ti = 1.54) than Ce (1.10).

The Co 2p spectra are displayed in Fig. 8b. A set of Co 2p peaks located at ca. 780 eV and 795 eV corresponding to Co $2p_{3/2}$ and Co $2p_{1/2}$ respectively. Each peak was the summation of signals from Co^{2+} and Co^{3+}. In Co_3O_4, Co^{2+} has higher binding energy than Co^{3+} [49]. From the deconvoluted spectra in Fig. 8b, it was concluded that the peaks at 779 eV and 794 eV with a small satellite signal around 788 eV correspond to Co^{3+}. The peaks at 781 eV and 797 eV were characteristic of Co^{2+} [50]. Detailed calculation from the deconvoluted peaks reveals that the intensity ratio of Co^{3+} and Co^{2+} was different in different catalysts. The surface atomic ratio of $(Co^{3+})_{xps}$

to $(Co^{3+} + Co^{2+})_{xps}$ was in following order Ce-Co > Ce-Zr-Co > Ce-Sn-Co > Ce-Ti-Co (Table 3). Since this sequence was consistent with the NO conversion performance, the Co^{3+} on the surface therefore acted as the active sites and its quantity determined the capability of catalytic NO conversion into NO_2. Combined with H_2-TPR results, we could concluded that Co^{3+} was more favorable to form in the highly dispersed Co_3O_4 species.

O 1s spectra were mainly composed of two components. The peak of O 1s named as O_α, with a binding energy of 528-530 eV, contributed to the lattice oxygen in the metal oxides [36]. The high binding 531-532 eV energy was attributed to the surface chemisorbed oxygen (O_β) [36]. We could find that the O 1s ionization features for all of the catalysts are very similar (Fig. 8c). Obviously, the ratios of chemisorbed oxygen to the whole type of oxygen were higher compared to Ce-Co (Table 3), which indicated that the doping of other cations was beneficial for the formation of chemisorbed oxygen.

In addition, the narrow spectra of Zr 3d, Sn 3d and Ti 2p are shown in Fig. 8d. The binding energy of Zr $3d_{5/2}$ (181.8 eV) in the Ce-Zr-Co was consistent with ZrO_2 (181.8 eV), indicating that Zr was mainly in a +4 oxidation state [51]. As for the XPS spectra of Sn 3d, the most of Sn was mainly in a +4 oxidation state because the binding energy of Sn $3d_{5/2}$ (486.2 eV) in Ce-Sn-Co was uniform in SnO_2 (486.2 eV) [52]. For Ce-Ti-Co, the binding energy of Ti $2p_{3/2}$ was 458.0 eV, which was lower that in TiO_2 (458.3 eV) but higher that in TiO (454.8 eV), indicating that Ti was in a +4 oxidation state and a small quantity on a +3 oxidation state [53].

Fig. 8

Table 3

3.6. Relationship between catalytic performance and catalysts properties

It was interesting that different supports could lead to different catalytic performance. In order to understand this question clearly, we attempted to correlate the activity with the above-mentioned characterizations, and the relationship between NO conversion (at 300 ^{o}C) and textural/structural/reducible properties was plotted in Fig. 9. As far as we know, for some important catalytic reactions, the increase of the specific surface area of support was beneficial to the dispersion of active species, which could lead the activity to increase; the activity enhanced with decreasing the grain size of catalysts. However, it could be noted from Fig. 9a, the activity couldn't relate to the BET surface area and the grain size very well, we took the dispersion states of Co_3O_4 and the oxygen vacancies into account. In our previous work [35], we demonstrated that oxygen vacancies were important to the activation of oxygen. Oxygen turned into superoxide ions on oxygen vacancies, superoxide ions could oxide NO for its' strong oxidation ability [54]. Furthermore, the dispersion states of the oxides was also a vital factor, Luo et al. [13] found the finely dispersed CuO species had the highest catalytic activity among the finely dispersed CuO, the bulk CuO and the Cu^{2+} in the CeO_2 lattice. Highly dispersed Co_3O_4 species provided more

NO adsorption sites and oxygen vacancy were responsible for O_2 activation. The NO-TPD profiles are shown in Fig. S1. The results demonstrated the highly dispersed Co_3O_4 species were favorable for the NO adsorption. In H_2-TPR results, the peak β was ascribed to the reduction of Co^{3+} to Co^{2+}, the lower reduction temperature may lead to increase the activity. Interestingly, these properties are well in agreement with the activity (Fig. 9b).

Fig. 9

4. Conclusion

This work focused on different doped metal cations on the structure, texture, reduction, dispersion states of cobalt species, oxygen vacancies, adsorption properties and catalytic performance of the $Co_3O_4/Ce_{0.8}M_{0.2}O_2$ ($M = Zr^{4+}$, Sn^{4+} and Ti^{4+}) samples for NO oxidation. The catalytic performance results indicated that Co was the active sites. Combined with the above analysis, the catalytic activity of Ce-Co oxides was due to the higher amount of highly dispersed Co_3O_4, the larger amount of oxygen vacancies and the excellent redox ability.

Acknowledgments

This work was financially supported by the Assembly Foundation of The Industry and Information Ministry of the People's Republic of China 2012 (543), the National Natural Science Foundation of China (U1162119), Science and Technology Support Program of Jiangsu Province (BE2014713), Natural Science Foundation of Jiangsu

Province (BK20140777), Scientific Research Project of Environmental Protection Department of Jiangsu Province (2013003), Research Fund for the Doctoral Program of Higher Education of China (20113219110009), Industry-Academia Cooperation Innovation Fund Projects of Jiangsu Province (BY2012025) and (BY2014004-10), Science and technology project of Nanjing (201306012).

References

[1] Z. B. Wu, R. B. Jin, Y. Liu and H. Q. Wang, *Catal. Commun.*, 2008, **9**, 2217.

[2] G. Madia, M. Koebel, M. Elsener and A Wokaun. *Ind. Eng. Chem. Res.*, 2002, **41**, 3512.

[3] W. S. Epling, L. E. Campbell, A. Yezerets, N. W. Currier and J. E. Parks II, *Catal. Rev. Sci. Eng.*, 2004, **46**, 163.

[4] B. J. Cooper, H. J. Jung and J. E. Thoss, *US Patent 4*, 902, 487, 1990.

[5] H. Takeuchi, M. Ando and N. Kizawa, *Ind. Eng. Chem. Process Des. Dev.*, 1977, **16**, 303.

[6] W. Cai, Q. Zhong, W. Zhao and Y. F. Bu, *Appl. Catal., B*, 2014, **158-159,** 258.

[7] J. Giménez-Mañogil, A. Bueno-López and A. García-García, *Appl. Catal., B*, 2014, **152-153**, 99.

[8] I. Atribak, A. Bueno-López, A. García-García and B. Azambre, *Phys. Chem. Chem. Phys.*, 2010, **12**, 13770.

[9] S. K. Megarajana, S. Rayalu, Y. Teraoka and N. Labhsetwar, *J. Mol. Catal. A*, 2014, **385** ,112.

[10] Z. Ren, Y. B. Guo, Z. H. Zhang, C. H. Liu and P. X. Gao, *J. Mater. Chem. A*, 2013, **1**,9897.

[11] M. Sanchez-Dominguez, L. F. Liotta, G. D. Carlo, G. Pantaleo, A. M. Venezia, C. Solans and M. Boutonnet, *Catal. Today*, 2010, **158**, 35.

[12] L. Qi, C. J. Tang, L. Zhang, X. J. Yao, Y. Cao, L. F. Liu, F. Gao, L. Dong and Y. Chen, *Appl. Catal., B*, 2012, **127**, 234.

[13] M. F. Luo, Y. P. Song, J. Q. Lu, X. Y. Wang and Z. Y. Pu, *J. Phys. Chem. C*, 2007, **111**, 12686.

[14] L. Meng, J. J. Lin, Z. Y . Pu, L. F. Luo, A. P. Jia, W. X. Huang, M. F. Luo and J. Q. Lu, *Appl. Catal., B*, 2012,**119-120**, 117.

[15] J. Z. Shyu, W. H. Weber and H. S. Gandhi, *J. Phys. Chem.*, 1988, **2**, 4964.

[16] M. Yan, T. Mori, J. Zou, F. Ye, D. R. Ou and J. Drennan, *Acta Mater.*, 2009, **57**, 722.

[17] F. Chen, J. J. Zhu, Y. Y. Zhan, X. Y. Lin, G. H. Cai, K. M. Wei and Q. Zheng, *Appl. Catal., A*, 2009, **363**, 208.

[18] T. Yuzhakova, V. Rakić, C. Guimon and A. Auroux, Chem. Mater., 2007, 19, 2970.

[19] B. Bonnetot, V. Rakic, T. Yuzhakova, C. Guimon and A. Auroux, Chem. Mater., 2008, 20, 1585.

[20] S. Somacescu, P. Osiceanu, J. M. C. Morenoa, L. Navarrete and J. M. Serra, Microporous Mesoporous Mater., 2013, 179, 78.

[21] M. F. Luo, J. Chen, L. S. Chen, J. Q. Lu, Z. C. Feng and C. Li, *Chem. Mater.*, 2001, **13**,197.

[22] T. Y. Li, S. J. Chiang, B. J. Liaw and Y. Z. Chen, *Appl. Catal., B*, 2011, **103**,143.

[23] W. T. Chen, K. B. Chen, M. F. Wang, S. F. Weng, C. S. Lee and M. C. Lin, *Chem. Commun.*, 2010, **46**, 3286.

[24] W. Cai, Q. Zhong, S. L. Zhang and W. Zhao, *Chem. Eng. J.*, 2014, **36**, 223.

[25] I. Dobrosz-Gómez, I. Kocemba and J. M. Rynkowski, *Appl. Catal., B*, 2008, **83**,

240.

[26] J. L. Ayastuy, A. Iglesias-González and M. A. Gutiérrez-Ortiz, *Chem.Eng. J.*, 2014, **244**,372.

[27] Y. Wen, C. Zhang, H. He, Y. Yu and Y. Teraoka, *Catal. Today*, 2007, **126**, 400.

[28] M. F. Irfan, J. H. Goo and S. D. Kim, *Appl. Catal., B*, 2008, **78**, 267.

[29] D. S. Kim, Y. H. Kim, J. E. Yie and E. D. Park, *Korean J. Chem. Eng.*, 2010, **27**, 49.

[30] L. J. Liu, Z. J. Yao, B. Liu and L. Dong, *J. Catal.*, 2010, **275**, 45.

[31] A. Martínez-Arias, M. Fernández-García, L. N. Salamanca, R. X. Valenzuela, J. C. Conesa and J. Soria, *Phys. Chem. B*, 2000, **104**, 4038.

[32] Q. Q. Jiang, G. L. Zhou, Z. X. Jiang and C. Li, *Sol. Energy*, 2014, **99**, 55.

[33] B. Bonnetot, V. Rakic, T. Yuzhakova, C. Guimon and A. Auroux, *Chem. Mater.*, 2008, **20**, 1585.

[34] J. R. McBride, K. C. Hass, B. D. Poindexter and W. H. Weber, *J. Appl. Phys.*, 1994, **76**, 2435.

[35] S. L. Zhang, H. Y. Li and Q. Zhong, *Appl. Catal., A*, 2012, **435-436**, 156.

[36] R. Si, Y. W. Zhang, S. J. Li, B. X. Lin and C. H. Yan, *J. Phys. Chem. B*, 2004, **108**, 12481.

[37] B. M. Reddy, P. Bharali and P. Saikia, *J. Phys. Chem. C*, 2008, **112**, 11729.

[38] Á. Kukovecz, Z. Kónya, D. Mönter, W. Reschetilowski and I. Kiricsi, J. *Mol. Struct.*, 2001, **563-564**, 403.

[39] L. Poul, N. Jouini and F. Fiévet, *Chem. Mater.* 2000, **12**, 3123.

[40] L. J. Liu, Y. Cao, W. J. Sun, Z. J. Yao, B. Liu, F. Gao and L. Dong, *Catal. Today*, 2011, **175**, 48.

[41] J. Y. Luo, M. Meng, X. Li, X. G. Li, Y. Q. Zha, T. D. Hu, Y. N. Xie and J. Zhang, *J. Catal.*, 2008, **254**, 310.

[42] P. Arnoldy and J.A. Moulijn, *J. Catal.*,1985, **93**, 38.

[43] M. Kang, M. W. Song and C. H. Lee, *Appl. Catal. A*, 2003, **251**, 143.

[44] C. W. Tang, C. C. Kuo, M. C. Kuo, C. B. Wang and S. H. Chien, *Appl. Catal., A*, 2006, **309**,37.

[45] L. F. Liotta, G. Di Carlo, G. Pantaleo, A. M. Venezia and G. Deganello, *Appl. Catal., B*, 2006, **66**, 217.

[46] L. Spadaro, F. Arena, M. L. Granados, M. Ojeda and J. L. G. Fierro, F. Frusteri, J. Catal., 2005, **234**, 451.

[47] A. Martínez-Arias, M. Fernández-García, O. Gálvez, J. M. Coronado, J. A. Anderson, J. C. Conesa, J. Soria and G. Munuera, *J. Catal.*, 2000, **195**, 207.

[48] E. Béche, P. Charvin, D. peranau, S. Abanades and G. Flamant, *Surf. Interface. Anal.*, 2008, **40**, 264.

[49] M. Yung, E. Holmgreen and U. Ozkan, *Catal. Lett.*, 2007, **118**, 180.

[50] Y. Ding, L. Zhu, A. Huang, X. Zhao, X. Zhang and H. Tang, *Catal. Sci. Technol.*, 2012, **2**, 1977.

[51] S. Velu, K. Suzuki, C. S. Gopinath, H. Yoshida and T. Hattori, *Phys. Chem. Chem. Phys.*, 2002, **4**, 1990.

[52] D. Shuttleworth, *J. Phys. Chem.*, 1980, **84**,1629.

[53] B. M. Reddy, P. Lakshmanan and A. Khan, *J. Phys. Chem. B*, 2004, **108**, 16855.

[54] Z. Zhao, X. G.Yang and Y. Wu, *Appl. Catal., B*,1996, **8**, 281.

Fig. 1. Comparing NO conversion over the supports and catalysts.

Fig. 2. XRD patterns of the synthesized catalysts.

Fig. 3. LRS of the supports (a) and the catalysts (b).

Fig. 4. UV-vis spectra of these catalysts.

Fig. 5. TEM and HRTEM patterns of the samples. (A) Ce-Co; (B) Ce-Zr-Co; (C) Ce-Sn-Co; (D) Ce-Ti-Co.

Fig. 6. N_2 adsorption-desorption isotherms (a) and pore size distributions (b) of the samples.

Fig. 7. H_2-TPR profiles of these catalysts.

Fig. 8. XPS spectra of (Ce 3d, Co 2p, O 1s, Zr 3d, Sn 3d and Ti 2p) of the catalysts.

Fig. 9. The relationship between the catalytic activity of NO oxidation (at 300 ^{o}C) and (a) textural and (b) structural/reducible properties.

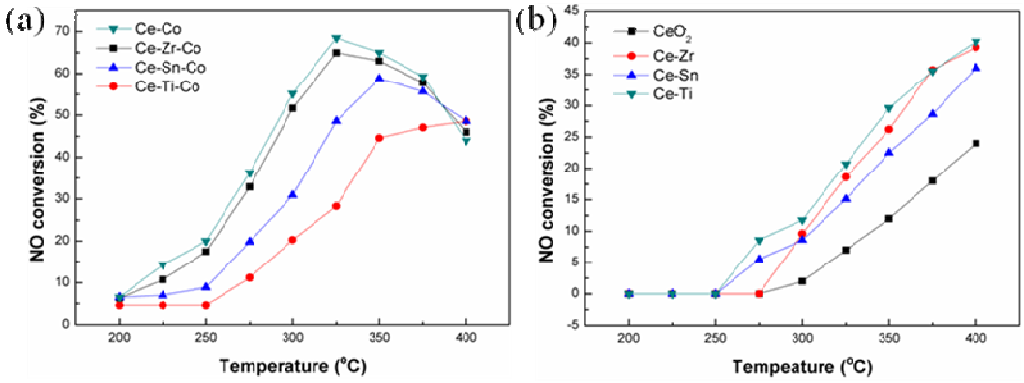

Fig.1 Comparing NO conversion over the supports and catalysts.

(Reaction conditions: 390 ppm NO, 8 % O_2, N_2 as balance gas, GHSV = 35,400 h^{-1}.)

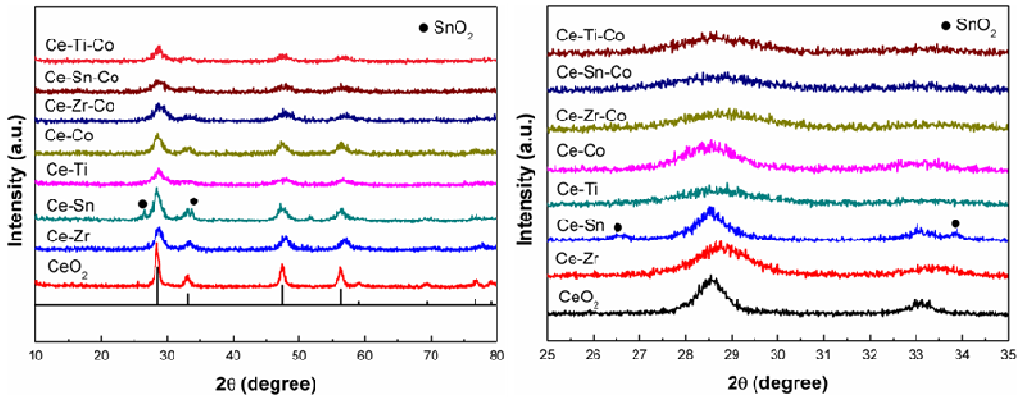

Fig. 2. XRD patterns of the synthesized catalysts.

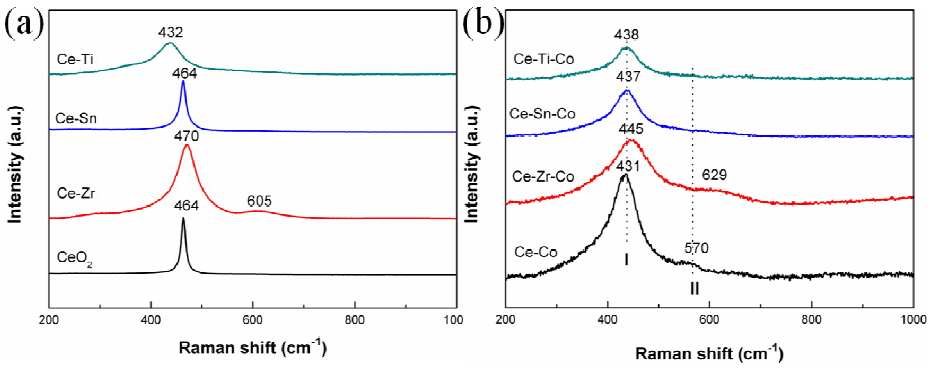

Fig. 3 LRS of the supports (a) and the catalysts (b).

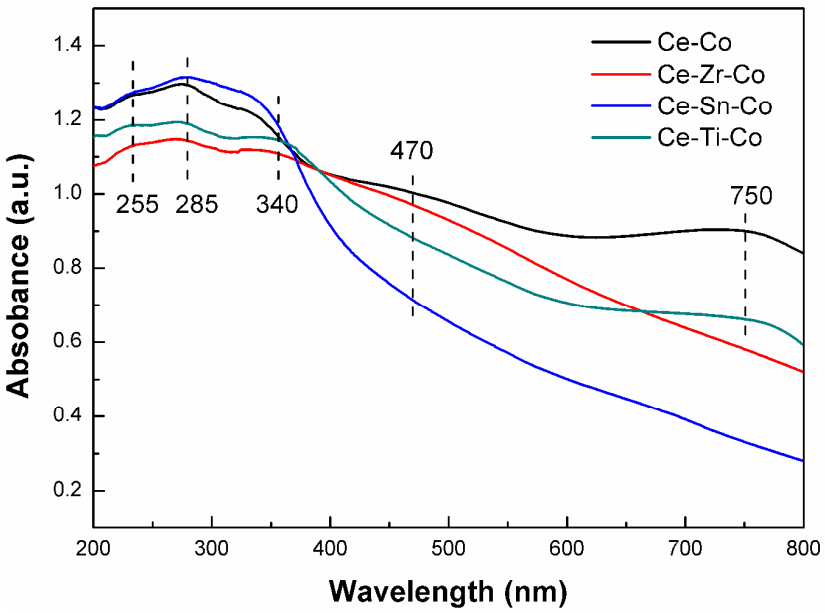

Fig. 4 UV-vis spectra of these catalysts.

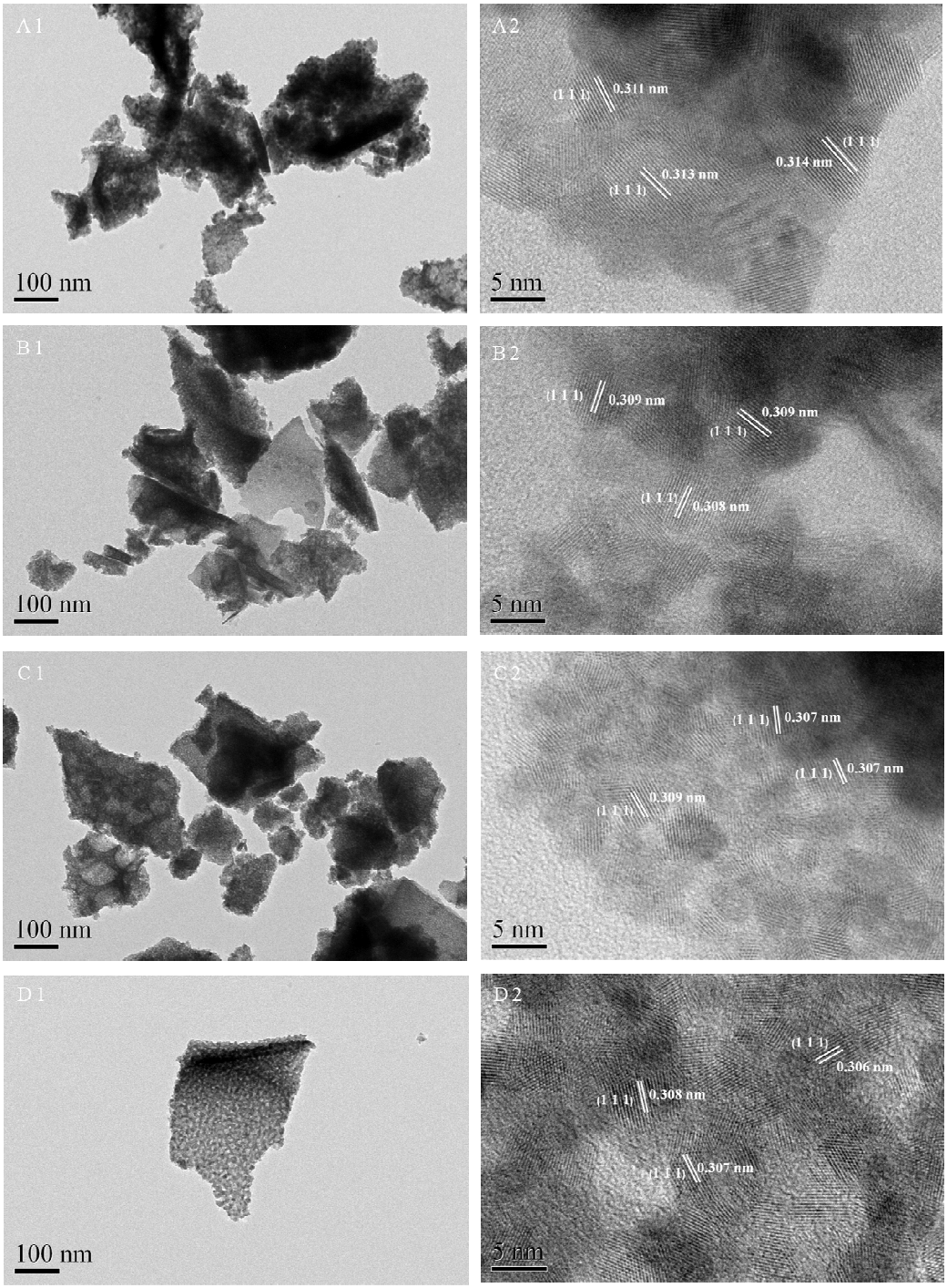

Fig. 5 TEM and HRTEM patterns of the samples. (A) Ce-Co; (B) Ce-Zr-Co; (C) Ce-Sn-Co; (D) Ce-Ti-Co.

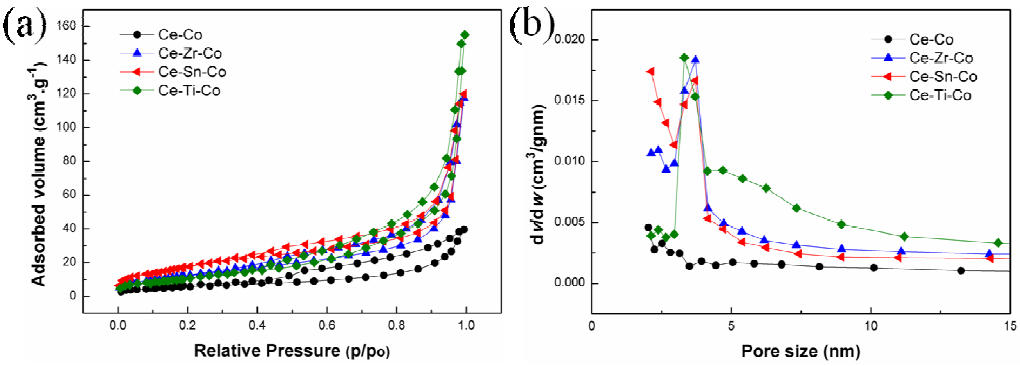

Fig. 6 N_2 adsorption-desorption isotherms (a) and pore size distributions (b) of the samples.

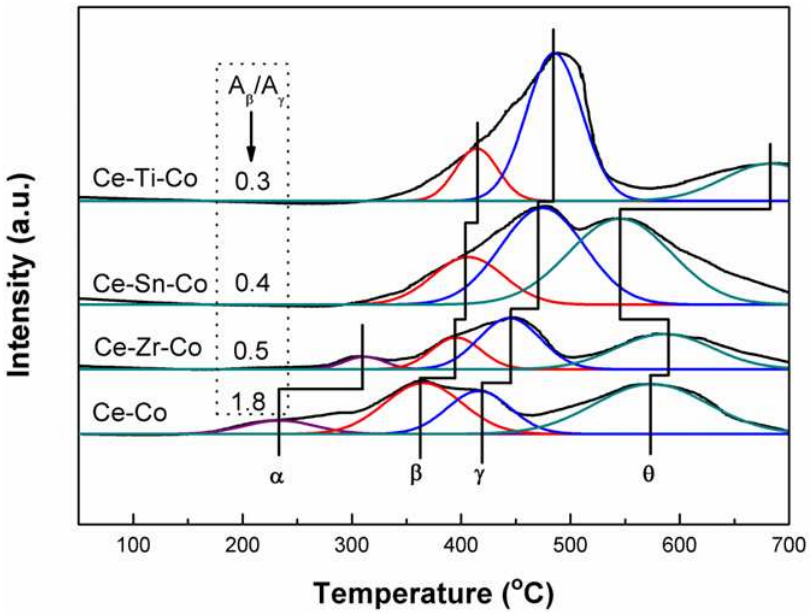

Fig. 7 H_2-TPR profiles of these catalysts.

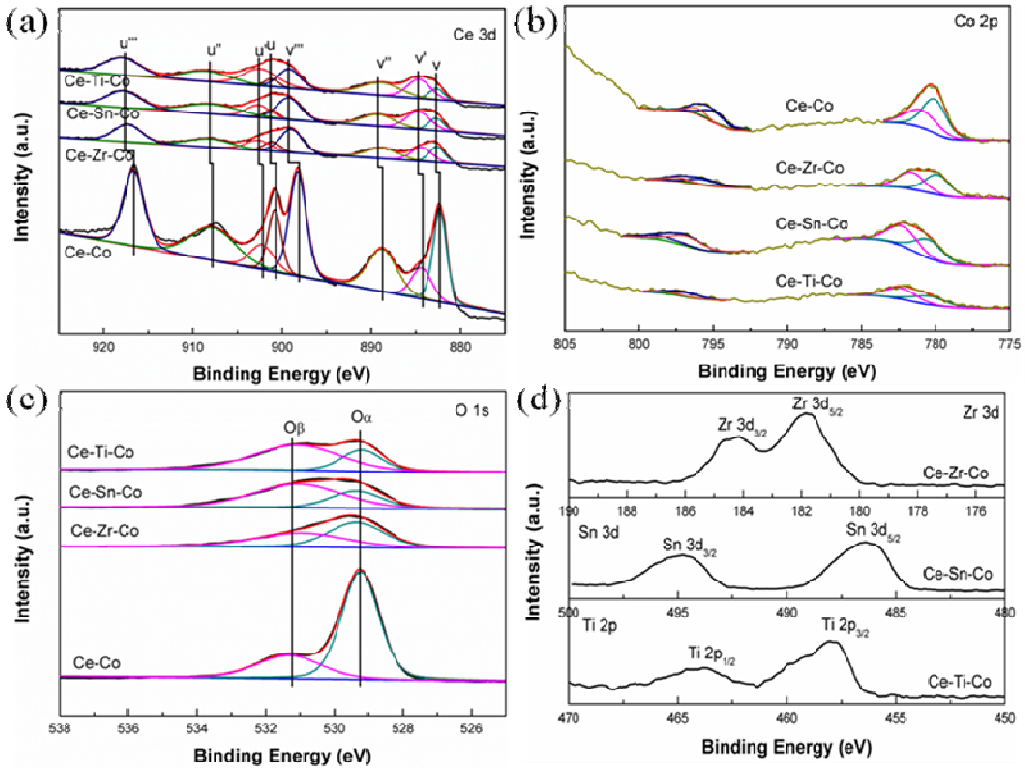

Fig. 8 XPS spectra of (Ce 3d, Co 2p, O 1s, Zr 3d, Sn 3d and Ti 2p) of the catalysts.

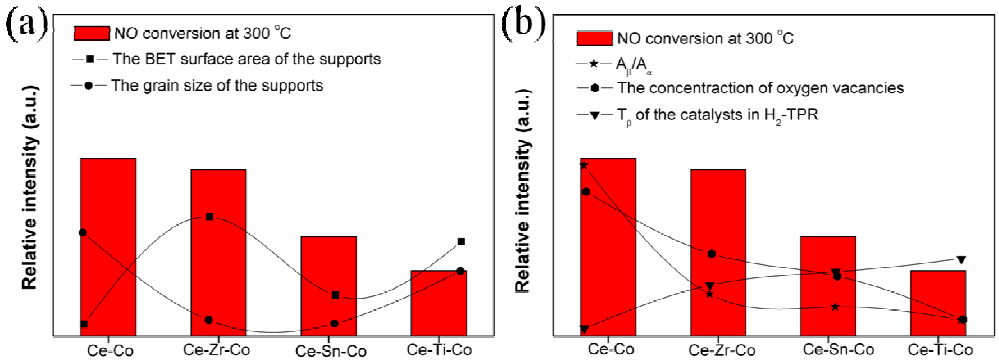

Fig. 9 The relationship between the catalytic activity of NO oxidation (at 300 °C) and (a) textural and (b) structural/reducible properties.

Table 1 Grain size, the position and FWHM of the main Raman line of the samples.

Sample	Grain size (nm)	Position of Raman line (cm^{-1})	FWHM of Raman line (cm^{-1})	A_{II}/A_I
CeO_2	16.4	464	9.6	/
Ce-Zr	7.7	470	52.3	/
Ce-Sn	15.4	464	15.5	/
Ce-Ti	5.5	432	69.9	/
Ce-Co	7.7	431	77.2	0.3113
Ce-Zr-Co	5.2	445	94.9	0.2098
Ce-Sn-Co	5.1	437	62.5	0.1327
Ce-Ti-Co	6.6	438	56.9	0.1024

Table 2 The surface area and pore structure parameters of the samples.

Sample	Ce-Co	Ce-Zr-Co	Ce-Sn-Co	Ce-Ti-Co
BET (m^2 g^{-1})	21	46	65	39
Pore size (nm)	6.9	11.3	10.8	13.8
Pore volume (mm^3 g^{-1})	66	192	188	257

Table 3 The bulk and surface composition of these catalysts (M = Zr, Sn, Ti).

Sample	Atomic ratio (%)						
	XRF (bulk)		XPS (surface)				
	Ce/M	Co/(Ce + M + Co)	Ce/M	Co/(Ce + M + Co)	$Co^{3+}/(Co^{3+} + Co^{2+})$	$Ce^{3+}/(Ce^{3+} + Ce^{4+})$	$O_\beta/(O_\alpha + O_\beta)$
Ce-Co	/	15.08 (15.00)	/	10.96	61.41	12.88	27.21
Ce-Zr-Co	4.08 (4.00)	14.98 (15.00)	4.42	16.99	55.20	20.35	47.26
Ce-Sn-Co	4.02 (4.00)	15.03 (15.00)	4.62	26.28	53.35	23.58	70.09
Ce-Ti-Co	4.01 (4.00)	15.01 (15.00)	4.51	15.33	49.28	30.42	71.12